

# Impact of local winter cooling on the melt of Pine Island Glacier, Antarctica

P. St-Laurent,<sup>1</sup> J. M. Klinck,<sup>1</sup> and M. S. Dinniman<sup>1</sup>

**Abstract.** The rapid thinning of the ice shelves in the Amundsen Sea is generally attributed to basal melt driven by warm water originating from the continental slope. We examine the hypothesis that processes taking place on the continental shelf contribute significantly to the interannual variability of the ocean heat content and ice shelf melt rates. A numerical model is used to simulate the circulation of ocean heat and the melt of the ice shelves over the period 2006–2013. The fine model grid (grid spacing 1.5 km) explicitly resolves the coastal polynyas and mesoscale processes. The ocean heat content of the eastern continental shelf exhibits recurrent decreases around September with a magnitude that varies from year to year. The heat loss is primarily caused by surface heat fluxes along the eastern shore in areas of low ice concentration (polynyas). The cold winter water intrudes underneath the ice shelves and reduces the basal melt rates. Ocean temperatures upstream (i.e. at the shelf break) are largely constant over the year and cannot account for the cold events. The cooling is particularly marked in 2012 and its effect on the ocean heat content remains visible over the following years. The study suggests that ocean-atmosphere interactions in coastal polynyas contribute to the interannual variability of the melt of Pine Island Glacier.

## 1. Introduction

The ice shelves of the Amundsen and Bellingshausen Seas are thinning at rates as high as  $6.8 \text{ m yr}^{-1}$ , the fastest observed around Antarctica [Pritchard *et al.*, 2012]. The unusually rapid thinning is generally attributed to basal melt driven by warm ocean water rather than iceberg calving or surface melt [Rignot *et al.*, 2013]. The West Antarctic Ice Sheet (adjacent to the Amundsen and Bellingshausen Seas) is particularly vulnerable to this process as much of it is grounded below the sea level. This part of the continent experienced large recessions in the past 1 Myr that yielded substantial increases in the global sea level [Naish *et al.*, 2009; Pollard and DeConto, 2009]. Recent studies suggest that most Amundsen Sea glaciers would be free of bed obstacles that could prevent further retreat [Rignot *et al.*, 2014] and that early stage collapse may have begun [Joughin *et al.*, 2014] assuming that present basal melt rates and warm ocean conditions are maintained in the future.

Ice volume budgets for the Amundsen embayment confirm that the ice flux changed considerably over the last decades. The discharge from Pine Island Glacier (PIG, see Fig. 1) increased dramatically between 1994 and 2008 before stabilizing in 2009 [Mouginot *et al.* [2014], their Fig. 4a). Although this variability may be related to glaciological processes (the grounding line reached the end of an ice plain around 2008), basal melt rates are known to be highly sensitive to ocean temperatures [Holland *et al.*, 2008]. Observations collected between 1994 and 2012 indicate that the volume of warm modified Circumpolar Deep Water (mCDW) present on the continental shelf also increased between 1994 and 2009 and decreased afterward [Dutrieux *et al.*, 2014].

One hypothesis to explain the interannual variability in mCDW is that large-scale atmospheric circulation patterns

control the onshelf flux of ocean heat and consequently the melt of ice shelves in the Amundsen Sea (a ‘remote control’, Thoma *et al.* [2008]; Steig *et al.* [2012]). Another hypothesis is that local processes (e.g., ocean heat loss in coastal polynyas) modulate the ocean heat content and thus the melt of ice shelves (e.g., Gwyther *et al.* [2014]; Khazendar *et al.* [2013]; Padman *et al.* [2012]; Holland *et al.* [2010]).

In this study we examine the latter hypothesis using a 3-D ice shelf-sea ice-ocean coupled model. In contrast with earlier numerical studies, the fine grid of the model explicitly resolves the polynyas and mesoscale processes over the entire Amundsen Sea. The model is forced with winds from the Antarctic Mesoscale Prediction System (AMPS, 10–20 km grid spacing) that resolve the large glacial valleys surrounding the Amundsen Sea. The numerical experiments focus on the period 2006–2013 when the volume of mCDW present on the continental shelf started to decrease [Dutrieux *et al.*, 2014].

The next section describes the numerical model and the experiments of the study. Then, we present results that support the view that local processes contribute to modulating the ice shelf melt. The last section summarizes the main results and discusses their significance in the context of global sea level rise.

## 2. Method

To simulate the conditions in the Amundsen Sea we employ a 3-D sea ice-ocean coupled model (Regional Ocean Model System, ROMS version 3.4, Shchepetkin and McWilliams [2005]; Budgell [2005]) thermodynamically-coupled to static ice shelves (with the three-equation formulation of Holland and Jenkins [1999] and transfer coefficients that are function of the friction velocity; see Dinniman *et al.* [2011]). The model domain is  $1400 \times 735 \text{ km}$  and covers the Amundsen Sea with a grid having a uniform horizontal spacing of 1.5 km (Fig. 1). The fine grid is necessary to resolve the baroclinic Rossby radius (about 5 km on the continental shelf), to properly represent the small coastal polynyas ( $O(100 \text{ km}^2)$ ) and the horizontal transport of ocean heat (e.g., Arthur *et al.* [2013]; St-Laurent *et al.* [2013], their Fig. 13).

<sup>1</sup>Center for Coastal Physical Oceanography, Old Dominion University, Norfolk, Virginia, USA.

The domain geometry is from IBCSO [Arndt *et al.*, 2013, sea floor] and BEDMAP-2 [Fretwell *et al.*, 2013, ice shelves] and includes Cosgrove, Pine Island, Thwaites, Crosson, Dotson and Getz ice shelves as well as most of Abbot (located at the edge of the domain, see Fig. 1). These two datasets are considerably more detailed than other products [e.g. R-Topo 1.5; Timmermann *et al.*, 2010] but they also show significant differences in the shape of certain ice shelf cavities (notably Crosson and PIG). The vertical dimension is discretized with 20 topography-following ( $\sigma$ ) levels with refinement near the surface. The ocean model uses constant diffusivities along the horizontal (biharmonic for momentum,  $3 \times 10^5 \text{ m}^4 \text{ s}^{-1}$ , and harmonic for scalars,  $2 \text{ m}^2 \text{ s}^{-1}$ ) and the  $k$ -profile parameterization in the vertical [Large *et al.*, 1994]. The sea ice component [Budgell, 2005; Hedström, 2009] combines the elastic-viscous-plastic rheology of Hunke and Dukowicz [1997] and thermodynamics [Mellor and Kantha, 1989] for one layer of ice and one layer of snow.

The numerical model is forced with daily-averaged winds from AMPS [Powers *et al.*, 2012] having a changing horizontal grid spacing of 20 km (years 2006–2008), 15 km (2009–2012), and 10 km (2013). The annually-averaged winds from these three periods are generally consistent despite the changes in grid spacing. The AMPS forecasts assimilate the data from three Automatic Weather Stations (AWS) installed in the Amundsen Sea in early 2011. Winds are not available for the first two months of 2006 so they were taken from the same months in 2007. Comparisons between AMPS and ERA-Interim [Dee *et al.*, 2011] for the other atmospheric fields show relatively small differences on monthly timescales. We thus use monthly-averages from ERA-Interim covering the years 2006–2013 for all atmospheric fields other than winds. The model uses bulk formulas to calculate surface fluxes from the simulated ocean conditions and the prescribed surface atmospheric conditions [Fairall *et al.*, 2003]. Tidal forcing is not included.

The lateral boundary conditions are restricted to climatologies in order to focus on the interannual variability generated locally. The lateral ocean boundary conditions are imposed as radiation-nudging [Marchesiello *et al.*, 2001] to a monthly climatology assembled from five day state estimates of a  $1/6^\circ$ -resolution sea ice-ocean model constrained by observations (Southern Ocean State Estimate, SOSE, data from 1 Jan. 2008 to 31 Dec. 2010; see Mazloff *et al.* [2010]). Lateral boundary conditions for sea ice are from a monthly climatology assembled from daily sea ice concentration data from the Advanced Microwave Scanning Radiometer (AMSR-E, 12.5 km grid spacing, data from 1 Jan. 2006 to 1 Oct. 2011; see Cavalieri *et al.* [2014]). Note that AMSR-E data became unavailable after October 2011.

The Thwaites Ice Tongue (TIT) is an extension of Thwaites ice shelf composed of landfast ice and partially-grounded icebergs (e.g., Tinto and Bell [2011]). It is a semi-permanent feature of the basin (see Scambos *et al.* [2001]) that acts as a barrier for the westward-drifting sea ice. In our simulations the TIT is represented as a static extension of Thwaites ice shelf that blocks the passage of sea ice while allowing the ocean to freely circulate underneath it. The shape of the TIT varies slightly from year to year but the model requires its geometry to be constant. To circumvent this limitation, we pick the central year of the simulation (2009) and define the horizontal extent of the TIT as the area around Thwaites where the sea ice concentration from AMSR-E is  $\geq 75\%$  year-round (Fig. 1). The thickness of the TIT is poorly known and set to a uniform value in the model (1 m) for simplicity. The heat fluxes through the TIT are always small (section 7) since the TIT is treated as an extension of Thwaites ice shelf [see Dinniman *et al.*, 2007].

The model starts from the SOSE fields on 1 January 2006 and is integrated in time for 16 years. The model atmospheric forcing covers the period 1 Jan. 2006 to 31 Dec. 2013 (eight years) and is repeated twice. The initial adjustment (spin-up) takes five years but for convenience we ignore the first eight years altogether and focus our analysis on the second eight years.

### 3. Model–data comparison

Field observations from the eastern side of the basin exhibit particularly warm water ( $> 1^\circ\text{C}$ ) along a large glacial trough (Eastern Trough, Fig. 1; see Dutrieux *et al.* [2014]). Comparison between the model and data indicates that the model reproduces the intrusion of mCDW and the general thermal structure (Fig. 2). The main deficiencies are an overly diffuse halo/thermocline, a warm bias of  $0.5^\circ\text{C}$  around 400 m in front of PIG, and a slight cold bias in the bottom layer. Bottom potential temperatures are  $\sim 1.1^\circ\text{C}$  in observations (Fig. 2c) and  $\sim 0.9^\circ\text{C}$  in the model (Fig. 2b; see also Fig. 3b). Basal melt rates are most sensitive to bottom temperatures because the bulk of the melt takes place near the grounding lines (see Supporting Information).

Conditions on the western side of the Amundsen Sea are generally colder with maximum potential temperatures around  $0.5^\circ\text{C}$  [Dutrieux *et al.*, 2014]. Comparison between the model and data collected along the ice shelf front (Fig. 3) indicates that the model captures the west–east gradient in temperature. The thin thermocline (a regional proxy being the  $2^\circ$  above freezing isotherm) shoals from 600 m at Carney Island to 400 m near PIG. The main differences between the model and the data are a cold bias at depth in the eastern part of the domain (as noted above) and a warm bias west of Siple Island (thermocline 100 m too shallow). We attribute the warm bias to the boundary condition prescribed at the western edge of the model (the  $2^\circ$  isotherm is too shallow in SOSE).

The basal melt rates vary considerably amongst the main seven ice shelves of the basin (Table 1). The melt rates are largest underneath Thwaites ice shelf and PIG with values of 21 and  $15 \text{ m yr}^{-1}$ , respectively. The model reproduces the main regional differences but underestimates the melt of Crosson and Dotson ice shelves and overestimates the melt of Cosgrove. Note that ice shelf melt rates are very sensitive to ocean temperatures [Holland *et al.*, 2008] or ice shelf topography [Little *et al.*, 2009] and that the model skill is better or comparable to previous modelling studies [e.g., Timmermann *et al.*, 2012; Schodlok *et al.*, 2012].

### 4. Interannual variability of mCDW on the continental shelf

In this section we use the model to investigate the variability in the heat content of the continental shelf. We specifically focus on four subdomains located within the Eastern Trough (boxes A–D, Fig. 1). Box A is located at the entrance of the trough and represents the conditions upstream of the ice shelves. Boxes B to D represent the conditions in front of Cosgrove and PIG. The heat content within the subdomains is defined as the volume integration of the model potential temperature  $\theta$  (in  $^\circ\text{C}$ ) averaged over blocks of five days. Note that this definition of the heat content allows for negative values wherever the water temperature is  $< 0^\circ\text{C}$ . We further divide each subdomain into an upper and a lower box representing the conditions above and below 250 meters, respectively. This depth horizon represents an arbitrary limit between the surface layers (that are heavily modified by surface fluxes) and the deeper layers.

The variability of the upper boxes is dominated by a large seasonal cycle in all the subdomains (Fig. 4a,c). The heat content reaches a maximum in January–February and a minimum around November. The seasonality of the upper box

is largely due to surface heat fluxes mediated by the seasonal sea ice cover (not shown). The heat content below 250 meters follows a different evolution. Upstream of the ice shelves (box A, Fig. 4b), the heat content gradually increases from 2006 to 2009 and decreases afterward (in qualitative agreement with the observations of *Dutrieux et al.* [2014]). The variability is considerably smaller than in the upper box. There is no obvious seasonality as peaks and troughs appear sometimes in summer and sometimes in winter.

In front of the ice shelves, the heat content of the lower box generally increases in 2006 and decreases in late 2012 (Fig. 4d). The timeseries exhibit abrupt declines in September of years 2006, 2007, 2012 and 2013. These events are more pronounced at box B (Cosgrove) but are also visible at box C and D (see September 2007, 2012 and 2013). A decrease of  $10 \times 10^{11} \text{ }^\circ\text{C m}^3$  is approximately equivalent to a  $0.3^\circ\text{C}$  decrease in the mean temperature of a box. We note that the overall variability is very different from the upstream box (A) and that boxes B,C,D tend to evolve together (Fig. 4b,d). In the next section we will focus on the origin of these cold events that affect Cosgrove and PIG.

## 5. Formation and circulation of the cold anomalies

We investigate the origin of the cold anomalies by examining the ocean temperature and circulation in the months prior to September. For this purpose we create a monthly climatology of the model results for the years 2006–2013. We specifically focus on the conditions at depth (250 meters) since they are closer to the conditions underneath the ice shelves.

The month of June is characterized by relatively warm temperatures ( $> -0.3^\circ\text{C}$  over the eastern trough) from the shelf break to PIG (Fig. 5a). The flow is eastward at the shelf break and becomes southward within the eastern trough. The streamlines converge in front of PIG to form a clockwise gyre [e.g., *Thurnherr et al.*, 2014]. In the following months the conditions at the shelf break stay relatively constant while the temperature along the coast becomes gradually cooler (Fig. 5b,c,d). The cooling is particularly vigorous in front of Cosgrove Ice Shelf and between Cosgrove and PIG (box C) with temperatures reaching  $-1.9^\circ\text{C}$  at the coast (Fig. 5b,c,d). The streamlines indicate that some of this cold water is transported southward and joins with the clockwise gyre located in front of PIG. In October the temperatures start to increase again along the eastern shore (Fig. 5e,f).

The sequence of events shown in Fig. 5 takes place every year but with different magnitude. The cooling is most apparent in September 2006, 2007, 2012 and 2013 (Fig. 4d). The recurrence of the phenomenon is illustrated in two movies (see ‘Supporting Information’) showing the heat content below 250 m and the temperature at 375 m depth, respectively. This depth horizon corresponds to the highest instrument on most moorings deployed in the Amundsen Sea.

We examine the formation of the cold anomalies in further detail with two transects located in front of Cosgrove ice shelf and between Cosgrove and PIG (magenta and cyan lines in Fig. 1, respectively). In both cases, near-freezing water appears around June at the surface near the ice shelf front/coastline (Fig. 6a,e). The cold water mass expands vertically and horizontally over the following months (Fig. 6a–h). By September, the  $-1^\circ\text{C}$  isotherm reaches the sea floor along the cyan transect (500 m depth, Fig. 6h). The results from these two transects are suggestive of large surface heat loss and cold water formation in front of Cosgrove and along the coastlines of box C.

The cold water mass expands sufficiently far offshore to affect the transport of heat within the southward coastal

current (Fig. 6d,h) that leads to the clockwise gyre of Pine Island Bay (Fig. 5). This sequence of events, from the formation of cold water inside boxes B-C to its advection within the gyre, is represented in the two movies in ‘Supporting Information’. The southward propagation of the cold anomaly is also represented by Hovmöller diagrams in Supporting Information. The signal propagates along the coast at a speed varying between 8 and  $15 \text{ cm s}^{-1}$ .

The passage of the cold anomaly in front of PIG is accompanied by a deepening of the isotherms between August and September (Fig. 6i,j). The  $-1^\circ\text{C}$  isotherm reaches down to 400 m in September which is sufficiently deep for the cold anomaly to affect the basal melt rates. Note that the strongly-sheared and surface-intensified flow at the ice shelf front contributes to deepening the isotherms through the thermal wind relationship. The characteristics of the flow (speed  $O(25 \text{ cm s}^{-1})$  near the surface, decreasing to  $\sim 0$  at  $\sim 550 \text{ m}$ , Fig. 6i,j) are in broad agreement with the observations of *Thurnherr et al.* [2014, their Fig. 6].

## 6. Heat budget for the coast of the eastern Amundsen Sea

We examine the cause of the annual cooling occurring along the coastlines (e.g., Figs. 5,6) by considering the heat budget of the boxes defined in Fig. 1:

$$\frac{\partial}{\partial t} \mathcal{H}_{\text{box}}(t) = S(t) + B(t) + I(t) + R(t), \quad (1)$$

where  $\mathcal{H}_{\text{box}}$  is a volume-integration of the model potential temperature (bottom to surface),  $S$  is the net surface heat flux,  $B$  represents the net horizontal heat transport across the lateral boundaries of a box, and  $I$  is the heat flux at the ice shelf-ocean interface (where the box is bounded by an ice shelf). The budget represented in Eq. 1 is constructed from 5-day averages of each term in the temperature equation (time-derivative, horizontal and vertical advection, horizontal and vertical diffusion). The averaged fields are interpolated from the original topography-following grid to the boxes of Fig. 1. A residual term  $R(t)$  is added to Eq. 1 to represent the errors arising from the interpolation and from horizontal diffusion of heat (neglected in Eq. 1; the horizontal diffusivity is only  $2 \text{ m}^2 \text{ s}^{-1}$ ).

The cooling occurring in boxes B and C (Figs. 5,6a–h) is represented by large negative values for  $\partial H/\partial t$  from March to October (Fig. 7a,b). In both boxes the negative  $\partial H/\partial t$  is primarily due to the surface heat fluxes  $S$ . This term remains significant during the period of heavy sea ice cover (austral winter) which suggests the presence of polynyas along the coast (see next section). The next term in importance is the lateral transport of heat ( $B$ ) that is generally positive and equivalent to an influx of warm water and/or an outflow of cold water. This term fluctuates over the year with the ocean circulation but it generally increases from August to November as the cold winter water produced in these boxes is gradually replaced by warmer water (Fig. 5). The other terms of the budget ( $I$ ,  $R$ ) are relatively small and play a secondary role in the seasonal cycle (Fig. 7a,b).

The heat budget for box D is qualitatively different than those of box B,C. The surface heat fluxes ( $S$ ) are still significant but have a secondary effect on the seasonal cycle. The budget is dominated by the lateral heat transport ( $B$ ) and by heat loss to the ice shelf (PIG,  $I$ ). The heat transport decreases by  $\sim 33\%$  between August and September and leads to a similar decrease in ice shelf melt ( $I$ ; in agreement with Fig. 6i,j). In the next section we will examine how the sea ice cover allows for the large surface heat loss and cooling along the eastern shore of the Amundsen Sea.

## 7. Heat loss within polynyas

Winter-time surface heat loss is normally mediated by sea ice that acts as a thermal insulator. Satellite images reveal, however, recurrent areas of open water (polynyas) along the eastern shore of the Amundsen Sea during winter (Mankoff *et al.* [2012], their Fig. 5; Scambos *et al.* [2001]). The polynyas are represented in the model by ice concentrations approaching zero and correspondingly large surface heat fluxes.

The general distribution of sea ice simulated by the model is compared to satellite observations in Fig. 8 (AMSR-E and SSM/I, Special Sensor Microwave Imager). The sea ice concentrations from SSM/I use the NASA Team (NT) algorithm on a 25 km grid [Cavalieri *et al.*, 2015]. The sea ice concentrations from AMSR-E use the Enhanced NASA Team (NT2) algorithm on a 12.5 km grid [Cavalieri *et al.*, 2014]. Both satellite datasets are gridded by summing and averaging the observational points whose center fall within a grid cell ('drop-in-bucket' method). A comparative study involving 21,600 ship-based observations around Antarctica [Beitsch *et al.*, 2015] shows that SSM/I with the NT algorithm underestimates sea ice concentrations by 13.9% during winter. AMSR-E with the NT2 algorithm overestimates concentrations by 4.7% during the same period.

The model and the two satellite estimates exhibit relatively low ice concentrations in front of Abbot, Cosgrove, and PIG (Fig. 8). This 'band' of low ice concentration is 10–50 km wide, or only a few grid points of the satellite data. A large polynya is also apparent on the lee side of the Thwaites Ice Tongue (the Amundsen Sea Polynya). This qualitative agreement between model and data suggests that the simulated ice cover is reasonably realistic. We note however that the three figures differ in absolute numbers. SSM/I concentrations are consistently lower than AMSR-E (by 10–15%). These large differences are consistent with the biases reported by Beitsch *et al.* [2015]. The model is similar to AMSR-E away from the shores but closer to SSM/I along the coasts. A more quantitative model–data comparison is further hindered by obvious differences in the shape of the coastlines and by artefacts from the 'bucket' averaging [especially in SSM/I; e.g., Martin *et al.*, 2004].

The general distribution of sea ice plays a critical role in the heat budget of the model. The loss of heat from the ocean surface is effectively zero except within the areas of low ice concentrations described previously (Fig. 7d). The polynyas allow a year-long exchange of heat between the ocean and the atmosphere inside box B and C (Fig. 7a,b). The surface heat fluxes are responsible for the cold surface winter water that is subsequently transported toward PIG. In the next section we examine the effect of the cold anomalies on the melt of PIG.

## 8. Effect of the cold anomalies on Pine Island Glacier

The impact of the cold events on PIG is examined in Fig. 9. We specifically focus on a potential density surface positioned approximately 20 m below the ice shelf ( $1027.525 \text{ kg m}^{-3}$ ). The ocean conditions prior to September are characterized by relatively warm temperatures underneath the ice shelf ( $> -0.5^\circ\text{C}$ ) and a vigorous outflow on the western side of the cavity (Fig. 9a, in agreement with the observations of [Thurnherr *et al.*, 2014]). In September the cold anomaly appears to propagate along the coast and within the southward current (described in section 5). It intrudes underneath PIG from its northern side and causes a temperature decrease of  $\sim -0.3^\circ\text{C}$  in the northern half of the ice shelf cavity (Fig. 9b). This cooling leads to a  $\sim 20\%$  decrease in the ice shelf melt rate between August and October (Fig. 7c). Some of the cold water does not enter the

ice shelf cavity and circulates along the ice shelf front before continuing westward (Fig. 6i,j).

This seasonal cooling occurs with a different magnitude over the years. The heat content of the ice shelf cavity (defined as in section 4 but with the volume integration limited to the cavity) shows small changes in September of years 2006 and 2011, and large decreases in 2007 and 2012 (Fig. 10a). The cooling of September 2012 corresponds to a 35% decrease in the heat content of the cavity. The basal melt of the ice shelf closely follows the heat content and drops from  $15 \text{ m yr}^{-1}$  to  $4 \text{ m yr}^{-1}$  in this particular year (Fig. 10b). The heat content partially recovers over the next 4 months but remains  $\sim 10\%$  lower than in the previous years, indicating that the cold events can have a lasting effect on the heat content and melt rates. The cold anomaly of September 2012 can be seen down to 600 m depth downstream of PIG (Fig. 11). Abnormally cold temperatures remain visible at 300 m depth until May 2013.

Mooring data and numerical simulations covering longer periods of time will be required to fully understand the interannual variability of ice shelf melt rates in the Amundsen Sea. We can nevertheless use the present model results for a preliminary investigation. The variations in the heat content of PIG/box D are primarily driven by the lateral transport of heat (Fig. 7c) which in turn depends on the heat content upstream and the ocean circulation. We thus define for our purpose the 'heat content upstream of PIG' as the heat content below 250 m in boxes B-C, and the 'volume transport upstream of PIG' as the depth-integrated flow across a gate positioned north of PIG (see Fig. 9).

Interannual variations in the heat content upstream seem to explain some of the variations in PIG's heat content (compare Figs. 10a and c) but certain discrepancies are apparent. The large heat loss in box B in September 2006 has no counterpart in PIG's heat content timeseries (Fig. 10a,c). We suggest that such discrepancies could be caused by interannual variations in the ocean circulation. The transport across the gate is relatively weak in September 2006 (Fig. 10d) which would effectively prevent the cold water from reaching the ice shelf cavity. Additional *in situ* observations will be required to confirm or invalidate the model results.

## 9. Discussion and Summary

Field observations from the last 20 years describe the warming and subsequent cooling of the water on the continental shelf of the Amundsen Sea [Dutrieux *et al.*, 2014]. The variability is often attributed to the large-scale atmospheric circulation influencing the onshelf flux of heat [Thoma *et al.*, 2008; Steig *et al.*, 2012]. Additional observations are required however to confirm that this mechanism is the sole control over the melt of the ice shelves (e.g., Wåhlin *et al.* [2013]). Our study suggests that local processes (surface heat loss in coastal polynyas) also modulate the heat content of the shelf and have a direct impact on ice shelf melt rates. Future modelling studies that aim to compare these two drivers should cover the entire range of variability at the shelf break and also resolve the coastal polynyas.

The importance of surface heat loss in coastal polynyas was highlighted in studies of Totten Glacier (another fast-melting glacier in Eastern Antarctica, Khazendar *et al.* [2013]; Guyther *et al.* [2014]) and in the Bellingshausen Sea [Padman *et al.*, 2012; Holland *et al.*, 2010]. Such small-scale coastal processes represent a formidable obstacle for realistic projections of future ice sheet mass balance and global sea level rise. The Pine Island Glacier polynya cannot be represented explicitly in state-of-the-art climate models whose grid spacing is  $O(10 \text{ km})$  and larger. Similarly, Antarctic ice sheet models often assume idealized ocean forcing and lack the ocean-atmosphere interactions described in this study (e.g., Nowicki *et al.* [2013]). A final caveat concerns the topography of the ice shelf cavities that changes over time and is not always properly constrained [see Fretwell *et al.*, 2013].

**Acknowledgments.** This research was supported by the National Science Foundation under Grant OCE-0927797 and by the Turing High Performance Computing cluster at Old Dominion University. The data for this study are available upon request to the corresponding author (Pierre St-Laurent, pierre@ccpo.odu.edu). The authors are grateful for the helpful suggestions provided by the reviewers.

## References

- Arndt, J. E., H. W. Schenke, M. Jakobsson, F. O. Nitsche, G. Buys, B. Goleby, M. Rebesco, F. Bohoyo, J. Hong, J. Black, R. Greku, G. Udintsev, F. Barrios, W. Reynoso-Peralta, M. Taisei, and R. Wigley (2013), The International Bathymetric Chart of the Southern Ocean (IBCSO) Version 1.0—A new bathymetric compilation covering circum-Antarctic waters, *Geophys. Res. Lett.*, *40*(12), 3111–3117, doi:10.1002/grl.50413.
- Årthun, M., P. Holland, and K. W. Nicholls (2013), Eddy-driven exchange between the open ocean and a sub-ice shelf cavity, *J. Phys. Oceanogr.*, *43*(11), 2372–2387, doi:10.1175/JPO-D-13-0137.1.
- Beitsch, A., S. Kern, and L. Kaleschke (2015), Comparison of SSM/I and AMSR-E sea ice concentrations with ASPeCt ship observations around Antarctica, *IEEE transactions on geoscience and remote sensing*, *53*(4), doi:10.1109/TGRS.2014.2351497.
- Budgell, W. P. (2005), Numerical simulation of ice-ocean variability in the Barents Sea region: Towards dynamical downscaling, *Ocean Dyn.*, *55*, 370–387, doi:10.1007/s10236-005-0008-3.
- Cavalieri, D., T. Markus, and J. C. Comiso (2014), AMSR-E/Aqua daily L3 12.5 km brightness temperature, sea ice concentration, & snow depth polar grids. Version 3 for 2006–2011, Boulder, Colorado USA: NASA DAAC at the National Snow and Ice Data Center, doi:10.5067/AMSR-E/AE.S112.003.
- Cavalieri, D. J., C. L. Parkinson, P. Gloersen, and H. Zwally (2015), Sea ice concentrations from Nimbus-7 SMMR and DMSP SSM/I-SSMIS passive microwave data, data from 2006–2013, Boulder, Colorado USA: NASA DAAC at the National Snow and Ice Data Center, doi:10.5067/8GQ8LZQVLOVL.
- Dee, D. P., S. M. Uppala, A. J. Simmons, P. Berrisford, P. Poli, S. Kobayashi, U. Andrae, M. A. Balmaseda, G. Balsamo, P. Bauer, P. Bechtold, A. C. M. Beljaars, L. van de Berg, J. Bidlot, N. Bormann, C. Delsol, R. Dragani, M. Fuentes, A. J. Geer, L. Haimberger, S. B. Healy, H. Hersbach, E. V. Holm, L. Isaksen, P. Kallberg, M. Kohler, M. Matricardi, A. P. McNally, B. M. Monge-Sanz, J.-J. Morcrette, B.-K. Park, C. Peubey, P. de Rosnay, C. Tavolato, J.-N. Thepaut, and F. Vitart (2011), The ERA-Interim reanalysis: configuration and performance of the data assimilation system, *Quarterly Journal of the Royal Meteorological Society*, *137*, 553–597, doi:10.1002/qj.828.
- Depoorter, M. A., J. L. Bamber, J. A. Griggs, J. T. Lenaerts, S. R. Ligtenberg, M. R. van den Broeke, and G. Moholdt (2013), Calving fluxes and basal melt rates of Antarctic ice shelves, *Nature*, p. 5, doi:10.1038/nature12567.
- Dinniman, M. S., J. M. Klinck, and W. O. Smith Jr. (2007), Influence of sea ice cover and icebergs on circulation and water mass formation in a numerical circulation model of the Ross Sea, Antarctica, *J. Geophys. Res.*, *112*(C11013), doi:10.1029/2006JC004036.
- Dinniman, M. S., J. M. Klinck, and W. O. Smith Jr. (2011), A model study of Circumpolar Deep Water on the west Antarctic Peninsula and Ross Sea continental shelves, *Deep Sea Res. II*, *58*, 1508–1523, doi:10.1016/j.dsr2.2010.11.013.
- Dutrieux, P., J. De Rydt, A. Jenkins, P. R. Holland, H. K. Ha, S. H. Lee, E. J. Steig, Q. Ding, E. P. Abrahamson, and M. Schroder (2014), Strong sensitivity of Pine Island ice-shelf melting to climatic variability, *Science*, *343*(174), 174–178, doi:10.1126/science.1244341.
- Fairall, C. W., E. F. Bradley, J. E. Hare, A. A. Grachev, and J. B. Edson (2003), Bulk parameterization of air-sea fluxes: Updates and verification for the COARE algorithm, *J. Clim.*, *16*, 571–591.
- Fretwell, P., H. D. Pritchard, D. G. Vaughan, J. L. Bamber, N. E. Barrand, R. Bell, C. Bianchi, R. G. Bingham, D. D. Blankenship, G. Casassa, G. Catania, D. Callens, H. Conway, A. J. Cook, H. F. J. Corr, D. Damaske, V. Damm, F. Ferraccioli, R. Forsberg, S. Fujita, Y. Gim, P. Gogineni, J. A. Griggs, R. C. A. Hindmarsh, P. Holmlund, J. W. Holt, R. W. Jacobel, A. Jenkins, W. Jokat, T. Jordan, E. C. King, J. Kohler, W. Krabill, M. Riger-Kusk, K. A. Langley, G. Leitchenkov, C. Leuschen, B. P. Luyendyk, K. Matsuoka, J. Mouginot, F. O. Nitsche, Y. Nogi, O. A. Nost, S. V. Popov, E. Rignot, D. M. Rippin, A. Rivera, J. Roberts, N. Ross, M. J. Siegert, A. M. Smith, D. Steinhage, M. Studinger, B. Sun, B. K. Tinto, B. C. Welch, D. Wilson, D. A. Young, C. Xiangbin, and A. Zirizzotti (2013), Bedmap2: improved ice bed, surface and thickness datasets for Antarctica, *The Cryosphere*, *7*, 375–393, doi:10.5194/tc-7-375-2013.
- Gwyther, D. E., B. K. Galton-Fenzi, J. R. Hunter, and J. L. Roberts (2014), Simulated melt rates for the Totten and Dalton ice shelves, *Ocean Science*, *10*, 267–279, doi:10.5194/os-10-267-2014.
- Hedström, K. S. (2009), Technical manual for a coupled sea-ice/ocean circulation model (Version 3), *Tech. rep.*, Arctic Region Supercomputing Center, Univ. Alaska Fairbanks, [https://www.myroms.org/wiki/images/3/3b/Manual\\_2010.pdf](https://www.myroms.org/wiki/images/3/3b/Manual_2010.pdf).
- Holland, D. M., and A. Jenkins (1999), Modeling thermodynamic ice-ocean interactions at the base of an ice shelf, *J. Phys. Oceanogr.*, *29*, 1787–1800.
- Holland, P. R., A. Jenkins, and D. M. Holland (2008), The response of ice shelf basal melting to variations in ocean temperature, *J. Clim.*, *21*, 2558–2572, doi:10.1175/2007JCLI1909.1.
- Holland, P. R., A. Jenkins, and D. M. Holland (2010), Ice and ocean processes in the Bellingshausen Sea, Antarctica, *J. Geophys. Res.*, *115*(C05020), doi:10.1029/2008JC005219.
- Hunke, E. C., and J. K. Dukowicz (1997), An elastic-viscoplastic model for sea ice dynamics, *J. Phys. Oceanogr.*, *27*, 1849–1867.
- Jacobs, S., A. Jenkins, H. Hellmer, C. Giulivi, F. Nitsche, B. Huber, and R. Guerrero (2012), The Amundsen Sea and the Antarctic Ice Sheet, *Oceanography*, *25*(3), 154–163, doi:10.5670/oceanog.2012.90.
- Jacobs, S. S., A. Jenkins, C. F. Giulivi, and P. Dutrieux (2011), Stronger ocean circulation and increased melting under Pine Island Glacier ice shelf, *Nat. Geosc.*, *4*, 519–523, doi:10.1038/ngeo1188.
- Joughin, I., B. E. Smith, and B. Medley (2014), Marine ice sheet collapse potentially under way for the Thwaites Glacier Basin, West Antarctica, *Science*, *334*, 735–738, doi:10.1126/science.1249055.
- Khazendar, A., M. P. Schodlok, I. Fenty, S. R. Ligtenberg, E. Rignot, and M. R. van den Broeke (2013), Observed thinning of Totten Glacier is linked to coastal polynya variability, *Nature Communications*, *4*, doi:10.1038/ncomms3857.
- Large, W. G., J. C. McWilliams, and S. C. Doney (1994), Oceanic vertical mixing: A review and a model with a nonlocal boundary layer parameterization, *Rev. Geophys.*, *32*(4), 363–403.
- Little, C. M., A. Gnanadesikan, and M. Oppenheimer (2009), How ice shelf morphology controls basal melting, *J. Geophys. Res.*, *114*(C12007), doi:10.1029/2008JC005197.
- Mankoff, K. D., S. S. Jacobs, S. M. Tulaczyk, and S. E. Stammerjohn (2012), The role of Pine Island Glacier ice shelf basal channels in deep-water upwelling, polynyas and ocean circulation in Pine Island Bay, Antarctica, *Annals of Glaciology*, *53*(60), 123–128, doi:10.3189/2012AoG60A062.
- Marchesiello, P., J. C. McWilliams, and A. Shchepetkin (2001), Open boundary conditions for long-term integration of regional oceanic models, *Ocean Modelling*, *3*, 1–20.
- Martin, S., R. Drucker, R. Kwok, and B. Holt (2004), Estimation of the thin ice thickness and heat flux for the Chukchi Sea Alaskan coast polynya from Special Sensor Microwave/Imager data, 1990–2001, *J. Geophys. Res.*, *109*(C10012), 15, doi:10.1029/2004JC002428.
- Mazloff, M. R., P. Heimbach, and C. Wunsch (2010), An eddy-permitting Southern Ocean state estimate, *J. Phys. Oceanogr.*, *40*(5), doi:10.1175/2009jpo4236.1.
- Mellor, G. L., and L. Kantha (1989), An ice-ocean coupled model, *J. Geophys. Res.*, *94*, 10,937–10,954.
- Mouginot, J., E. Rignot, and B. Scheuchl (2014), Sustained increase in ice discharge from the Amundsen Sea Embayment, West Antarctica, from 1973 to 2013, *Geophys. Res. Lett.*, *41*, 1576–1584, doi:10.1002/2013GL059069.

**Table 1.** Model–data comparison for the basal melt rates in meters of ice. PIG is Pine Island Glacier.

Reference	Abbot m yr <sup>-1</sup>	Cosgrove m yr <sup>-1</sup>	PIG m yr <sup>-1</sup>	Thwaites m yr <sup>-1</sup>	Crosson m yr <sup>-1</sup>	Dotson m yr <sup>-1</sup>	Getz m yr <sup>-1</sup>
Observed <sup>a</sup>	2.72 ± 0.7	3.74 ± 0.89	15.96 ± 2.38	15.22 ± 3.87		9.47 ± 0.83	4.09 ± 0.68
Observed <sup>b</sup>	1.85 ± 0.7	3.04 ± 0.8	17.61 ± 1	19.24 ± 1	12.9 ± 1	8.48 ± 0.7	4.67 ± 0.4
Model <sup>c</sup>	1.84 ± 0.1	6.97 ± 0.5	15.16 ± 1	21.02 ± 2	5.0 ± 0.2	4.07 ± 0.5	7.62 ± 1

<sup>a</sup> Years 2007–2009 [Depoorter et al., 2013]. Crosson and Dotson are combined.

<sup>b</sup> Years 2007–2008 [Rignot et al., 2013].

<sup>c</sup> Years 2007–2008. The ± represents the standard deviation of annually-averaged values during the period 2006–2013.

- Naish, T., R. Powell, R. Levy, G. Wilson, R. Scherer, F. Talarico, L. Krissek, F. Niessen, M. Pompilio, T. Wilson, L. Carter, R. DeConto, P. Huybers, R. McKay, D. Pollard, J. Ross, D. Winter, P. Barrett, G. Browne, R. Cody, E. Cowan, J. Crampton, G. Dunbar, N. Dunbar, F. Florindo, C. Gebhardt, I. Graham, M. Hannah, D. Hansaraj, D. Harwood, D. Helling, S. Henrys, L. Hinnov, G. Kuhn, P. Kyle, A. Laufer, P. Maffioli, D. Magens, K. Mandernack, W. McIntosh, C. Millan, R. Morin, C. Ohneiser, T. Paulsen, D. Persico, I. Raine, J. Reed, C. Riesselman, L. Sagnotti, D. Schmitt, C. Sjunneskog, P. Strong, M. Taviani, S. Vogel, T. Wilch, and T. Williams (2009), Obliquity-paced Pliocene West Antarctic ice sheet oscillations, *Nature*, *458*, 322–329, doi:10.1038/nature07867.
- Nakayama, Y., M. Schroder, and H. H. Hellmer (2013), From circumpolar deep water to the glacial meltwater plume on the eastern Amundsen Shelf, *Deep-Sea Res. I*, *77*, 50–62, doi:10.1016/j.dsr.2013.04.001.
- Nowicki, S., R. A. Bindschadler, A. Abe-Ouchi, A. Aschwanden, E. Bueller, H. Choi, J. Fastook, G. Granzow, R. Greve, G. Gutowski, U. Herzfeld, C. Jackson, J. Johnson, C. Khroulev, E. Larour, A. Levermann, W. H. Lipscomb, M. A. Martin, M. Morlighem, B. R. Parizek, D. Pollard, S. F. Price, D. Ren, E. Rignot, F. Saito, T. Sato, H. Seddik, H. Seroussi, K. Takahashi, R. Walker, and W. L. Wang (2013), Insights into spatial sensitivities of ice mass response to environmental change from the SeaRISE ice sheet modeling project I: Antarctica, *J. Geophys. Res.*, *118*, 1–23, doi:10.1002/jgrf.20081.
- Padman, L., D. P. Costa, M. S. Dinniman, H. A. Fricker, M. E. Goebel, L. A. Huckstadt, A. Humbert, I. Joughin, J. T. Lenaerts, S. R. Ligtenberg, T. Scambos, and M. R. van den Broeke (2012), Oceanic controls on the mass balance of Wilkins Ice Shelf, Antarctica, *J. Geophys. Res.*, *117*(C01010), doi:10.1029/2011JC007301.
- Pollard, D., and R. M. DeConto (2009), Modelling West Antarctic ice sheet growth and collapse through the past five million years, *Nature*, *458*, 329–333, doi:10.1038/nature07809.
- Powers, J. G., K. W. Manning, D. H. Bromwich, J. J. Casano, and A. M. Cayette (2012), A decade of Antarctic science support through AMPS, *Bulletin of the American Meteorological Society*, November, 1699–1712, doi:10.1175/bams-d-11-00186.1.
- Pritchard, H. D., S. R. Ligtenberg, H. A. Fricker, D. G. Vaughan, M. R. van den Broeke, and L. Padman (2012), Antarctic ice-sheet loss driven by basal melting of ice shelves, *Nature*, *484*, 502–505, doi:10.1038/nature10968.
- Rignot, E., S. Jacobs, J. Mouginot, and B. Scheuchl (2013), Ice-shelf melting around Antarctica, *Science*, *341*, 266–270, doi:10.1126/science.1235798.
- Rignot, E., J. Mouginot, M. Morlighem, H. Seroussi, and B. Scheuchl (2014), Widespread, rapid grounding line retreat of Pine Island, Thwaites, Smith, and Kohler glaciers, West Antarctica, from 1992 to 2011, *Geophys. Res. Lett.*, *41*, 3502–3509, doi:10.1002/2014gl060140.
- Scambos, T., B. Raup, and J. Bohlander (2001), Images of Antarctic Ice Shelves (years 2006–2013), Boulder, Colorado USA: National Snow and Ice Data Center, <http://dx.doi.org/10.7265/N5NC5Z4N>.
- Schodlok, M. P., D. Menemenlis, E. Rignot, and M. Studinger (2012), Sensitivity of the ice-shelf/ocean system to the sub-ice-shelf cavity shape measured by NASA IceBridge in Pine Island Glacier, west Antarctica, *Annals of Glaciology*, *53*(60), 156–162, doi:10.3189/2012AoG60A073.
- Shchepetkin, A. F., and J. C. McWilliams (2005), The Regional Oceanic Modeling System (ROMS): A split-explicit, free-surface, topography-following-coordinate oceanic model, *Ocean Model.*, *9*, 347–404, doi:10.1016/j.ocemod.2004.08.002.
- St-Laurent, P., J. M. Klinck, and M. S. Dinniman (2013), On the role of coastal troughs in the circulation of warm Circumpolar Deep Water on Antarctic Shelves, *J. Phys. Oceanogr.*, *43*(1), 14, doi:10.1175/jpo-d-11-0237.1.
- Steig, E. J., Q. Ding, D. S. Battisti, and A. Jenkins (2012), Tropical forcing of Circumpolar Deep Water inflow and outlet glacier thinning in the Amundsen Sea embayment, West Antarctica, *Annals of Glaciology*, *53*(60), doi:10.3189/2012AoG60A110.
- Thoma, M., A. Jenkins, D. Holland, and S. Jacobs (2008), Modelling Circumpolar Deep Water intrusions on the Amundsen Sea continental shelf, Antarctica, *Geophys. Res. Lett.*, *35*(L18602), doi:10.1029/2008GL034939.
- Thurnherr, A. M., S. S. Jacobs, P. Dutrieux, and C. F. Giulivi (2014), Export and circulation of ice cavity water in Pine Island Bay, West Antarctica, *J. Geophys. Res.*, *119*, 1754–1764, doi:10.1002/2013jc009307.
- Timmermann, R., A. Le Brocq, T. Deen, E. Domack, P. Dutrieux, B. Galton-Fenzi, H. Hellmer, A. Humbert, D. Jansen, A. Jenkins, A. Lambrecht, K. Makinson, F. Niederjasper, F. Nitsche, O. A. Nost, L. H. Smedsrud, and W. H. Smith (2010), A consistent dataset of Antarctic ice sheet topography, cavity geometry, and global bathymetry, *Earth System Science Data Discuss.*, *2*(2), 261–273, doi:10.5194/essd-2-261-2010.
- Timmermann, R., Q. Wang, and H. H. Hellmer (2012), Ice-shelf basal melting in a global finite-element sea-ice/ice-shelf/ocean model, *Annals of Glaciology*, *53*(60), 303–314, doi:10.3189/2012AoG60A156.
- Tinto, K. J., and R. E. Bell (2011), Progressive unpinning of Thwaites Glacier from newly identified offshore ridge: Constraints from aerogravity, *Geophys. Res. Lett.*, *38*(L20503), doi:10.1029/2011GL049026.
- Wählin, A. K., O. Kalén, L. Arneborg, G. Björk, G. K. Carvajal, H. K. Ha, T. W. Kim, S. H. Lee, J. H. Lee, and C. Stranne (2013), Variability of warm deep water inflow in a submarine trough on the Amundsen Sea shelf, *J. Phys. Oceanogr.*, *43*, 2054–2070, doi:10.1175/JPO-D-12-0157.1.

Corresponding author: P. St-Laurent, Center for Coastal Physical Oceanography, Old Dominion University, 4111 Monarch Way, Suite 301, Norfolk, VA 23508, USA. (pierre@ccpo.odu.edu)

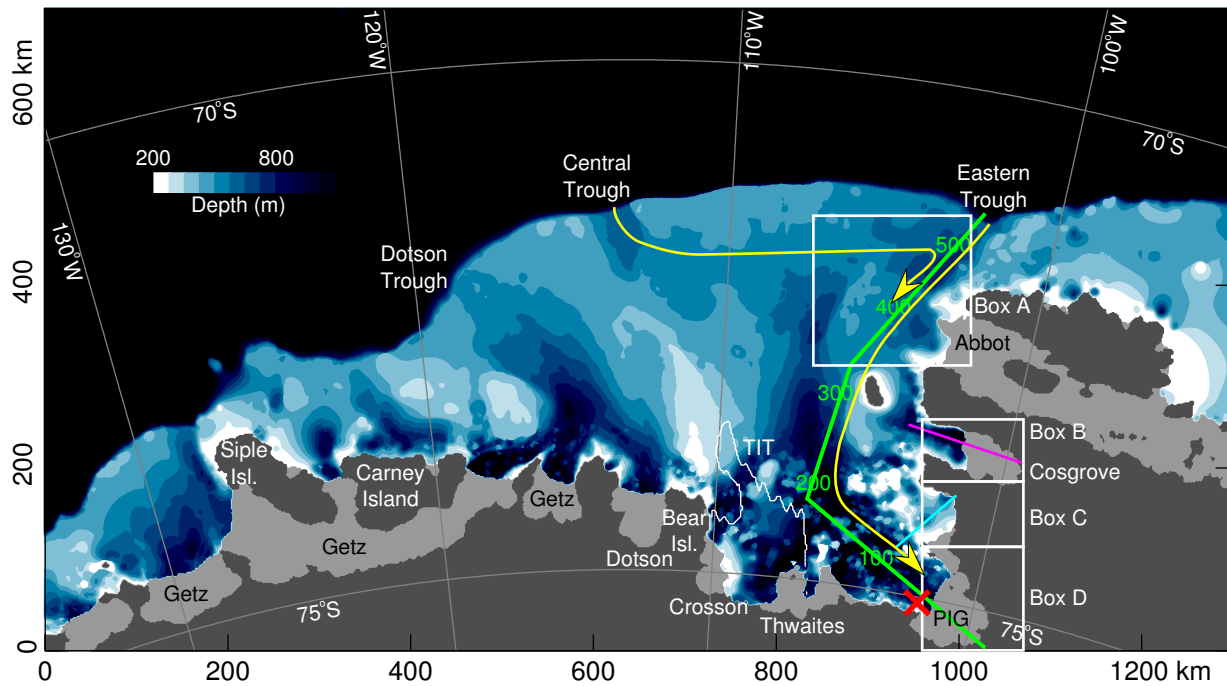


**Figure 1.** Model domain with the main ice shelves labeled. Color shading represents isobaths every 75 m. TIT is Thwaites Ice Tongue and PIG is Pine Island Glacier. The white boxes are the subdomains representing the eastern Amundsen Sea. The green line is the transect of Fig. 2 with distance in km from the ice shelf front (green numbers). The magenta and cyan lines represent the transect of Fig. 6a,b,c,d and Fig. 6e,f,g,h, respectively. The yellow arrows are the pathways of CDW intrusions [Nakayama *et al.*, 2013]. The red symbol is the location of the model grid point for the temperature timeseries shown in Fig. 11.

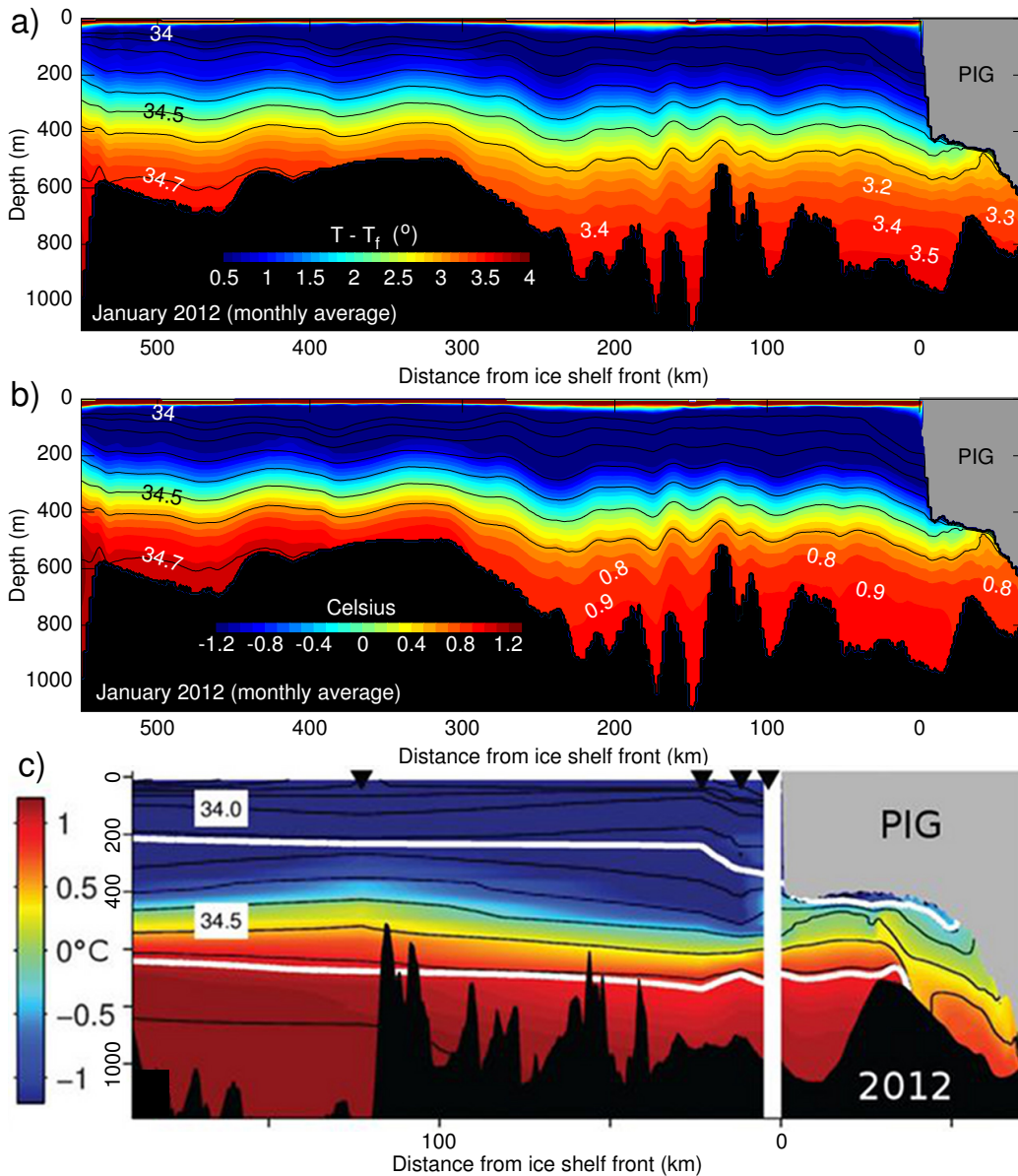


**Figure 2.** Temperature along the eastern trough (green line in Fig. 1). (a)  $T - T_f$  is the *in situ* temperature above the *in situ* freezing temperature. The black lines are isohalines every 0.1 psu. Results are averaged over January 2012. The model should be compared to *Jacobs et al.* [2011, their Fig. 2]. (b) Same as a but for potential temperature. (c) Same as b but from observations [*Dutrieux et al.*, 2014, their Fig. 3b, used with permission]. The temperatures inside the cavity are taken from a numerical simulation [see *Dutrieux et al.*, 2014]. Note the different horizontal scale in b and c.

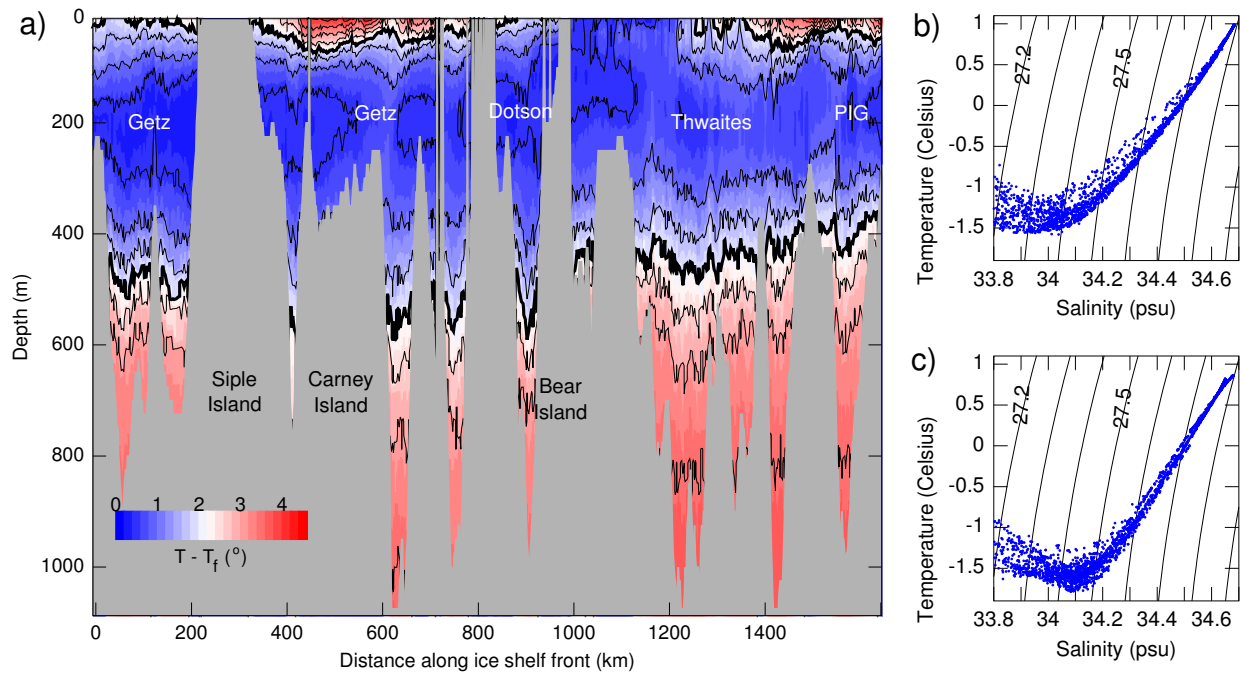


**Figure 3.** Simulated temperature along the ice shelf front (see Fig. 1; results are averaged over January 2007). (a)  $T - T_f$  is the *in situ* temperature above the *in situ* freezing temperature. The black contour lines highlight the isotherms (interval  $0.5^\circ$ , with  $2^\circ$  isotherm in bold). The model should be compared to *Jacobs et al.* [2012, their Fig. 2]. (b) Potential temperature–Salinity diagram for the conditions east of Dotson Ice shelf. The black contour lines represent potential density ( $\text{kg m}^{-3}$ ) referenced to the surface. (c) Same as b but west of Dotson Ice Shelf.

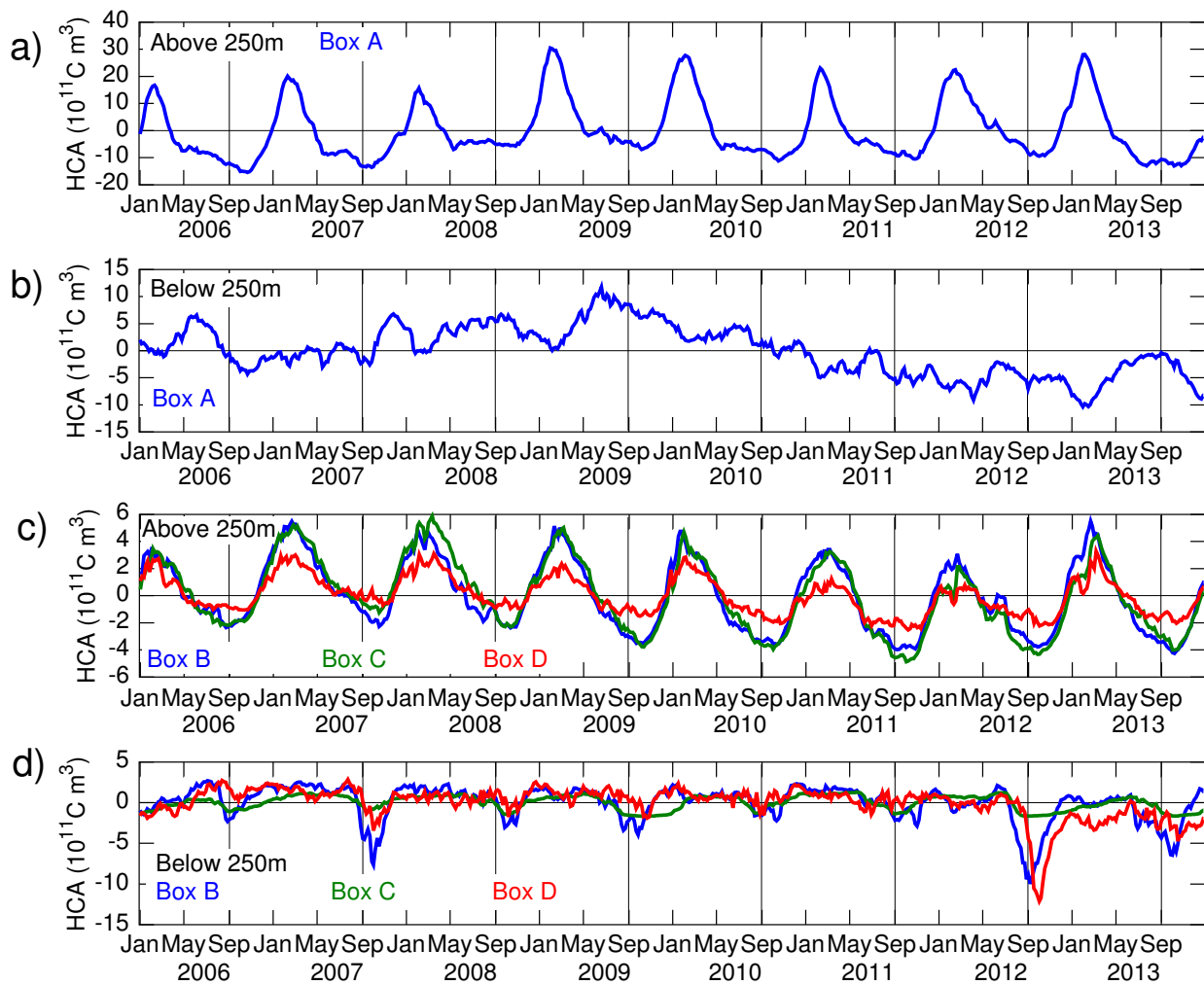


**Figure 4.** Heat content anomalies (HCA) within subdomains of the eastern Amundsen Sea (box A–D, see Fig. 1). The horizontal black line represents the mean value of the timeseries. (a) Heat content for the upper 250 meters of box A. (b) Same as a but for 250 meters to the bottom. (c) Same as a but for boxes B–D. (d) Same as b but for boxes B–D.

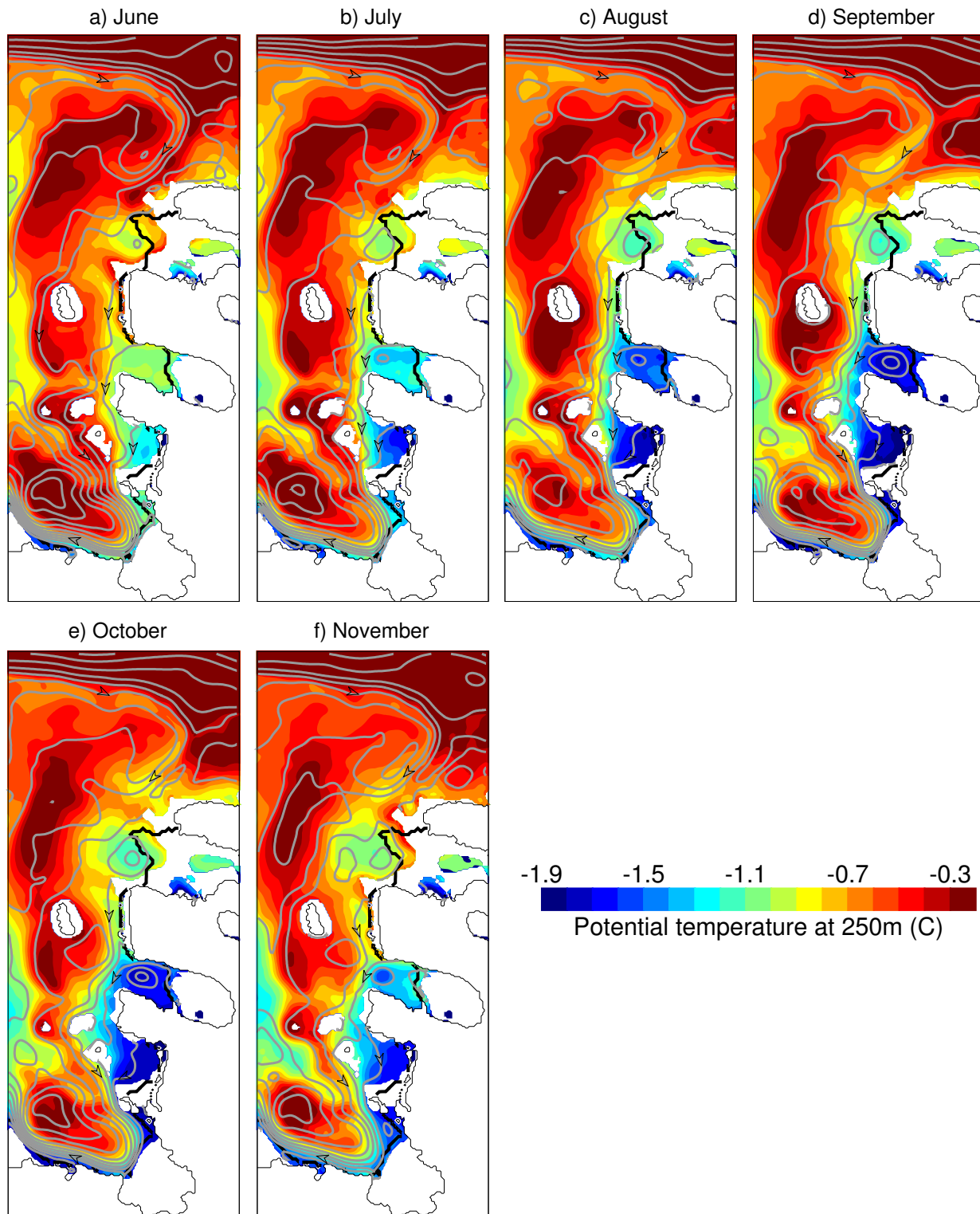


**Figure 5.** Formation and circulation of the cold anomalies (monthly climatology for years 2006–2013). The shading is the potential temperature at 250 m. The streamlines represent the mean ocean circulation at the same depth (interval  $500 \text{ m}^2 \text{ s}^{-1}$ ). Areas that are land or ice shelf at 250 m are masked with solid white. The thick (thin) black line is the ice shelf front (grounding line).

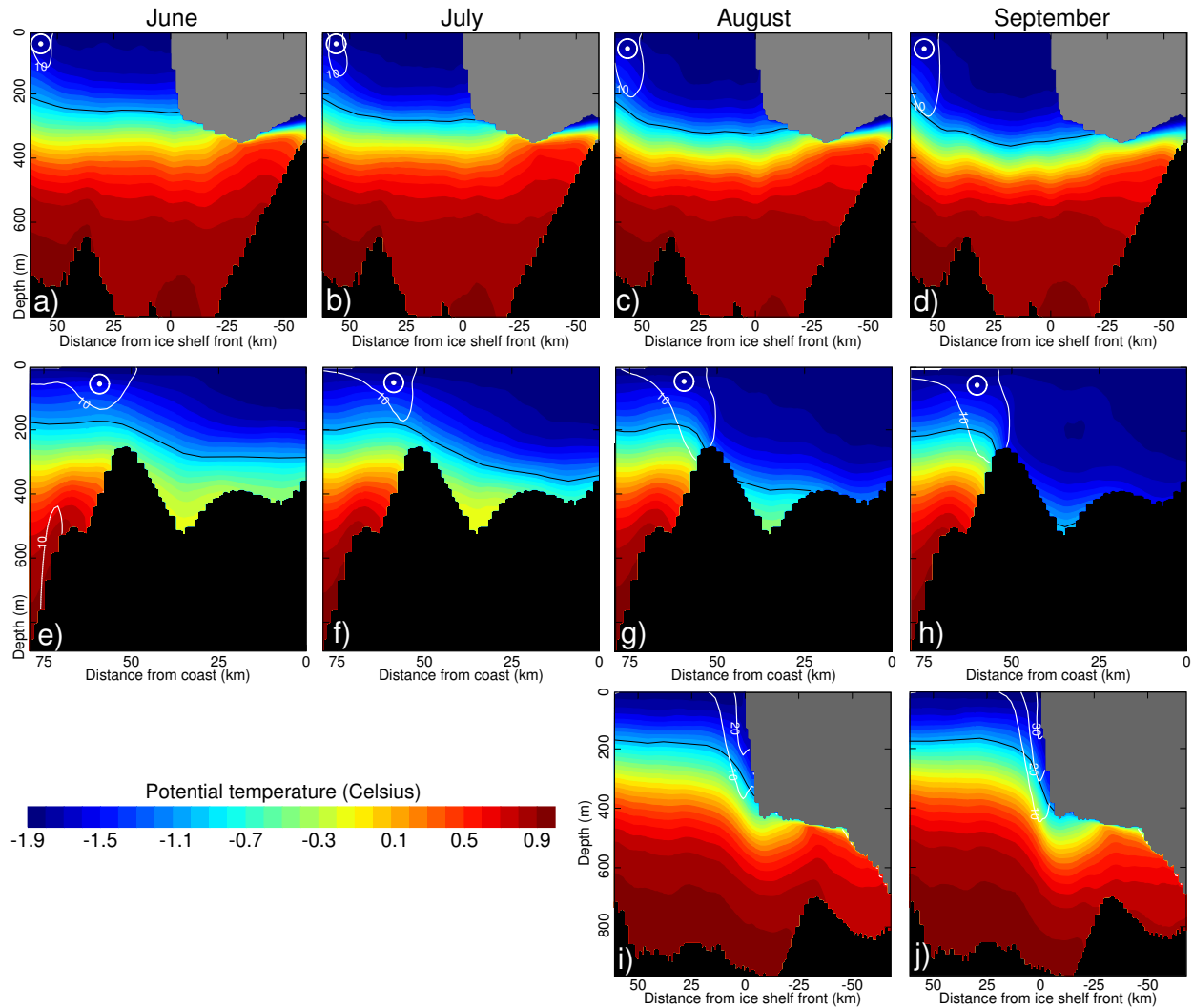


**Figure 6.** Cooling in front of Cosgrove ice shelf (a,b,c,d), between Cosgrove and Pine Island Glacier (e,f,g,h), and in front of PIG (i,j). See Fig. 1 for the location of the transects (magenta, cyan and green lines respectively). The black contour line is the  $-1^{\circ}\text{C}$  isotherm. The white contour lines represent the flow perpendicular to the transect (positive/southward out of page; isolines of 10, 20 and 30  $\text{cm s}^{-1}$  are shown). The southward coastal current is indicated by the symbol  $\odot$ .

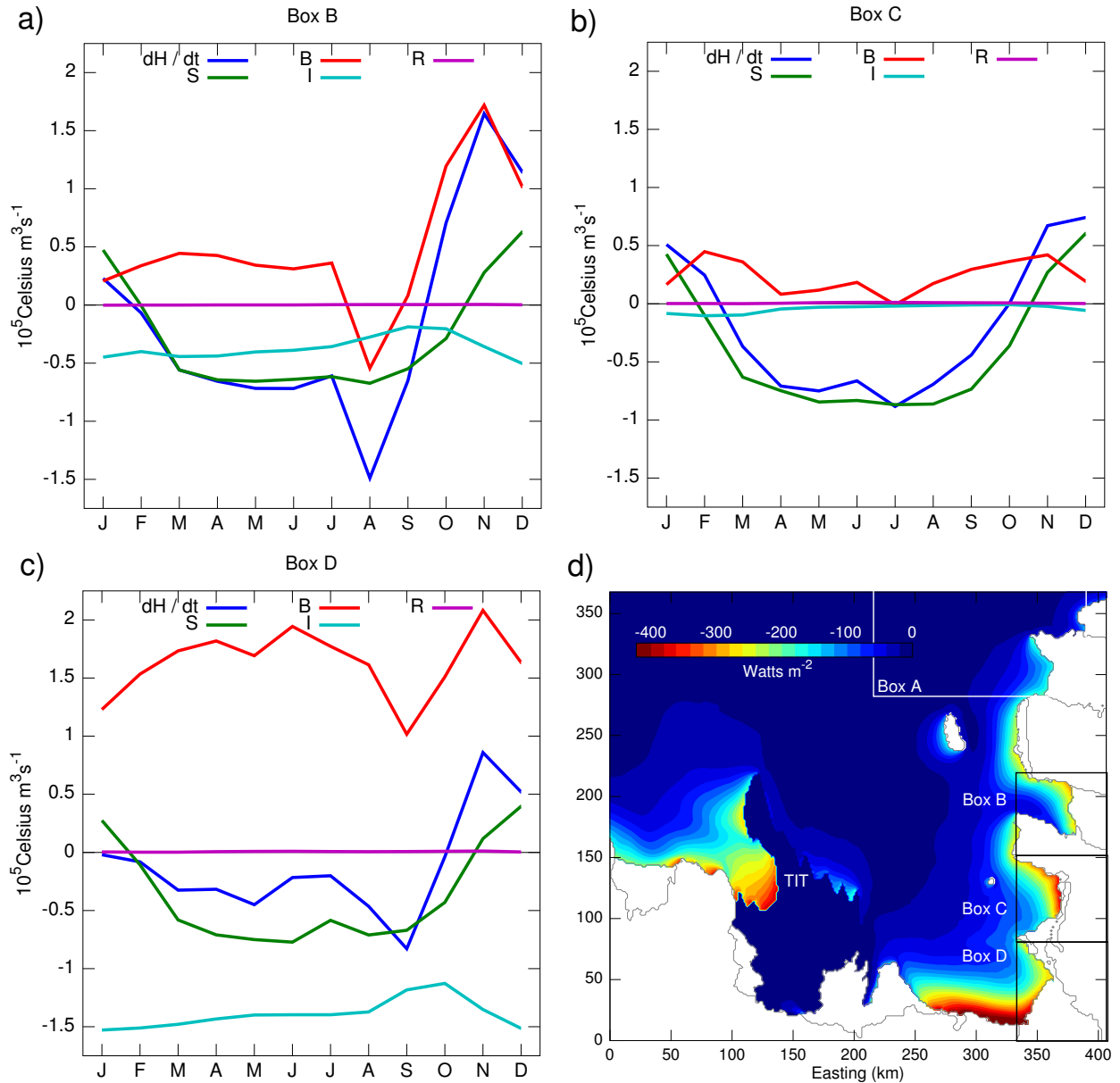


**Figure 7.** Seasonal heat budget along the eastern shore of the Amundsen Sea (Eq. 1). The seasonal cycle corresponds to a monthly average of years 2006–2013. (a,b,c) Budget for box B, C, and D (respectively; see Fig. 1). The budget is for the entire water column (bottom to surface). (d) Net heat flux at the surface of the ocean ( $< 0$  where the ocean loses heat) during July–August–September. The spatial distribution should be compared to Fig. 8a. TIT is Thwaites Ice Tongue. The black contour line is the grounding line.

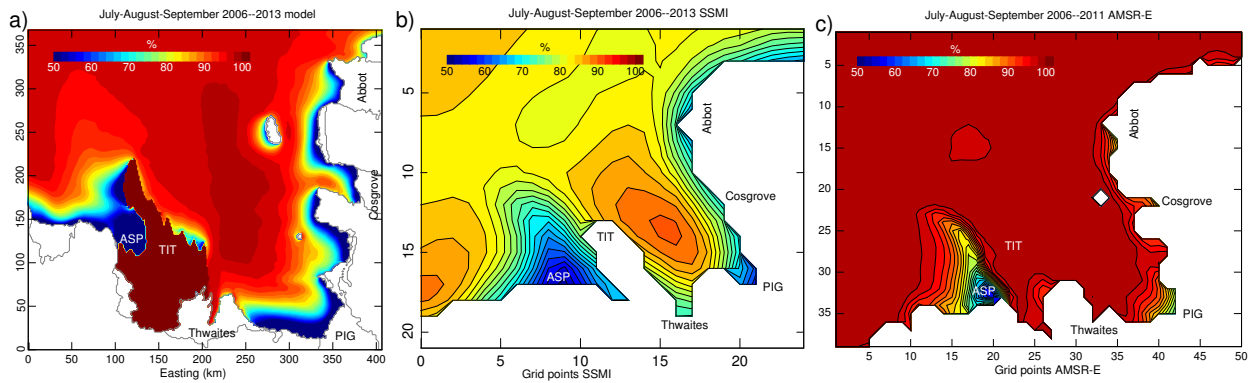


**Figure 8.** Average sea ice concentration during winter (July–August–September). (a) Modeled concentration for years 2006–2013. (b) Same as a but from SSMI. (c) Same as a but from AMSR-E and for years 2006–2011. ASP is Amundsen Sea Polynya, TIT is Thwaites Ice Tongue, and PIG is Pine Island Glacier.

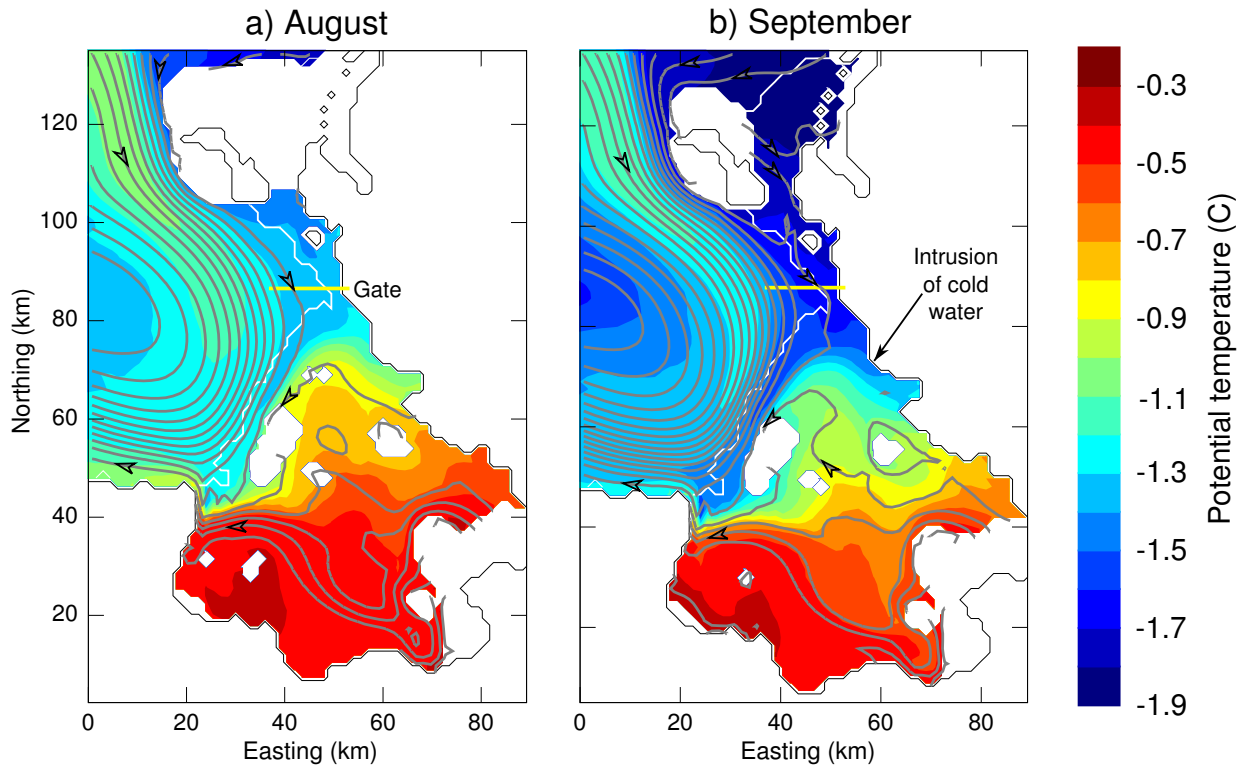


**Figure 9.** Intrusion of cold winter water inside the ice shelf cavity of Pine Island Glacier. (a) Model potential temperature (shading) and ocean circulation (streamlines, interval  $250 \text{ m}^2 \text{ s}^{-1}$ ) on a density surface ( $1027.525 \text{ kg m}^{-3}$ ). The fields are averaged over August 2006–2013. The black (white) line is the grounding line (ice shelf front). The yellow line is the gate used in Fig. 10d. Areas where the isopycnal intersects the sea floor/ice shelf are in solid white. (b) Same as a but for September.

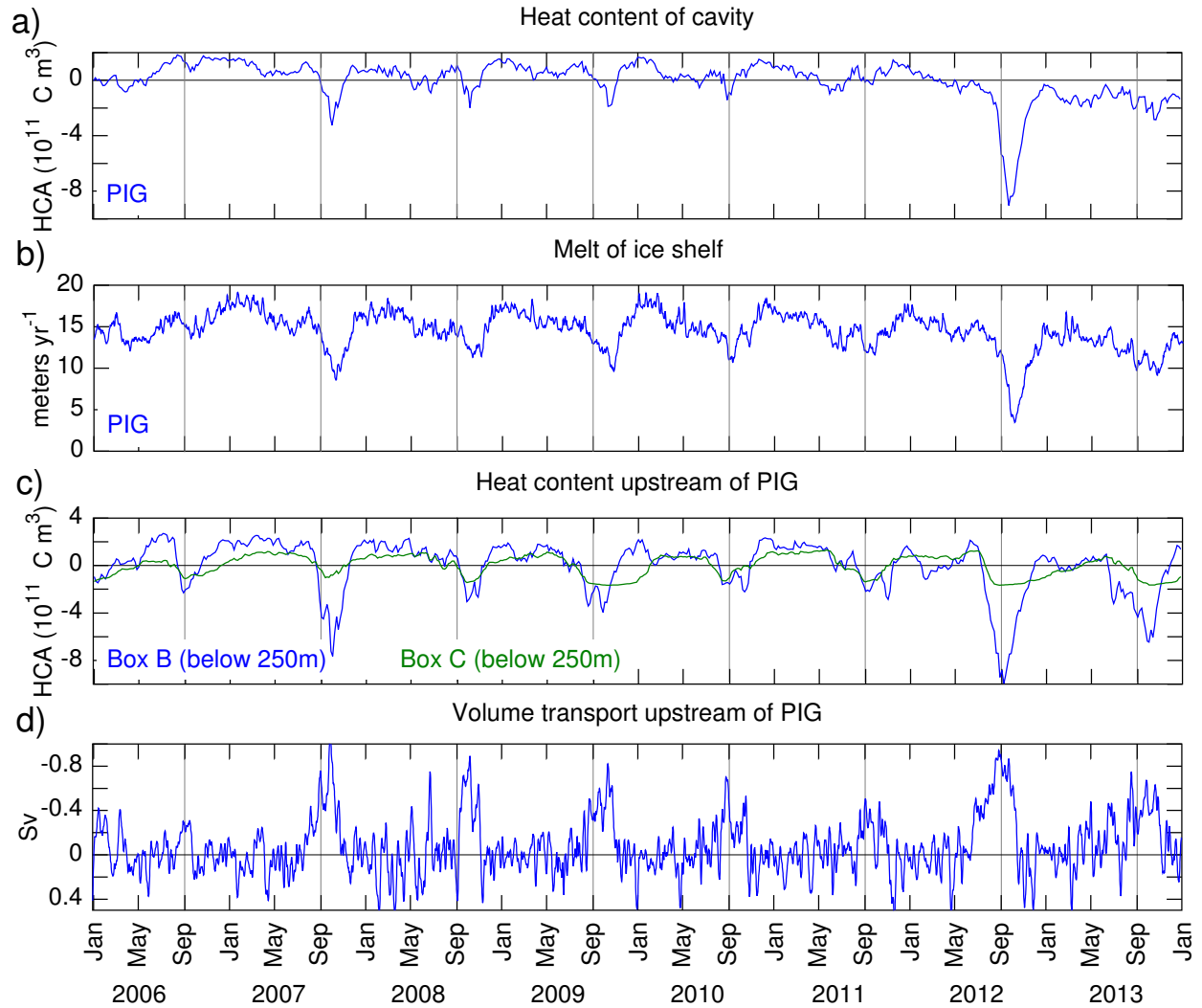


**Figure 10.** Heat content and melt of Pine Island Glacier (PIG). (a) Heat content based on potential temperature integrated over the ice shelf cavity. The mean value has been subtracted from the timeseries. HCA is Heat Content Anomaly. (b) Basal melt rate of the ice shelf. (c) Same as a but for boxes B,C and depths greater than 250 m. (d) Volume transport across a gate located upstream of PIG (see Fig. 9;  $1 Sv = 10^6 m^3 s^{-1}$ ). The transport is negative southward. The timeseries in b,d were smoothed with a 10 days low-pass filter.

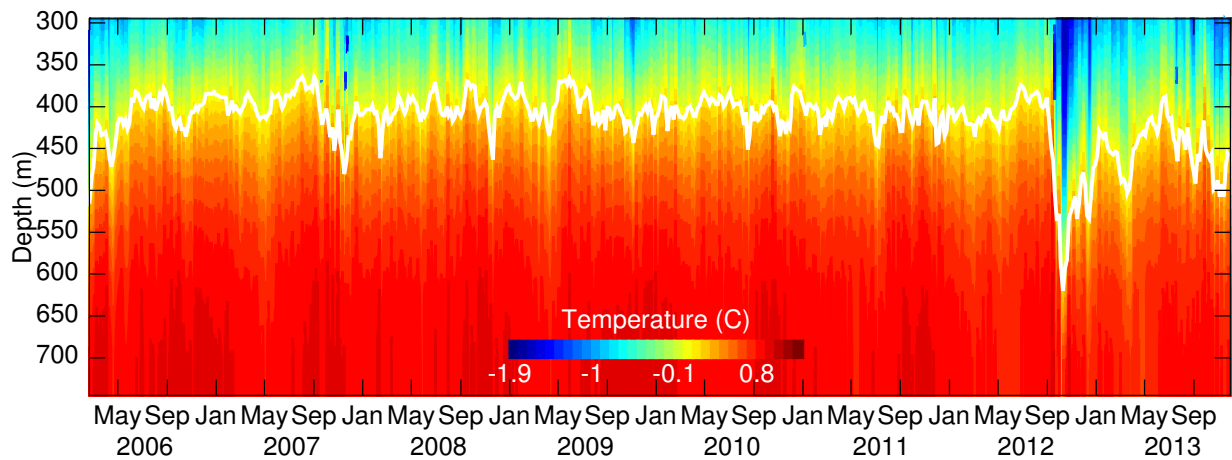


**Figure 11.** Model potential temperature downstream of Pine Island Glacier (75.055°S, 102.154°W; see Fig. 1). The white contour line is the 0°C isotherm.